Optical Materials 32 (2010) 643–647

Contents lists available at ScienceDirect

Optical Materials

journal homepage: www.elsevier.com/locate/optmat

# XAFS analysis and luminescent properties of ZnS:$Mn^{2+}$ nanoparticles and nanorods with cubic and hexagonal structure

Jian Cao [a,b], Jinghai Yang [c,*], Yongjun Zhang [c], Yaxin Wang [c], Lili Yang [c], Dandan Wang [a,b], Yang Liu [c], Xiaoyan Liu [c], Zhi Xie [d]

[a] Key Laboratory of Excited State Physics, Changchun Institute of Optics, Fine Mechanics and Physics, Chinese Academy of Sciences, 3888 Eastern Nan-Hu Road, Changchun 130033, PR China
[b] Graduate School of Chinese Academy of Sciences, Beijing 100049, PR China
[c] The Institute of Condensed State Physics, Jilin Normal University, Siping 136000, PR China
[d] National Synchrotron Radiation Laboratory, University of Science and Technology of China, Hefei, Anhui 230029, PR China

ARTICLE INFO

*Article history:*
Received 19 August 2009
Received in revised form 10 December 2009
Accepted 9 January 2010

*Keywords:*
ZnS:$Mn^{2+}$
Nanoparticles
Nanorods
XAFS
Luminescence

ABSTRACT

ZnS:$Mn^{2+}$ nanocrystals (NCs) were synthesized by a simple solvothermal method at 180 °C in different solvents. The NCs prepared in ethanol yielded cubic nanoparticles (NPs) with diameters of 10–15 nm. The NCs prepared in ethylenediamine and water (1:1 in volume ratio) yielded hexagonal nanorods (NRs) with diameters of 8–10 nm. X-ray absorption fine structure (XAFS) measurements were carried out to probe the local environment surrounding the Mn ions in the NPs and the NRs. The results showed that Mn ions were incorporated into the ZnS lattice substituting the Zn sites. The yellow–orange emission from the $Mn^{2+}$ $^4T_1$–$^6A_1$ transition was observed, its intensity relative to the blue–green emission increased from NPs to NRs. The surface effect was the main factor affecting the thermal and optical stability of NCs. The fluorescence lifetime of the $Mn^{2+}$ emission for the NPs and NRs was 0.662 and 0.224 ms, respectively.



## 1. Introduction

Zinc sulfide (ZnS) is an important II–VI semiconductor, which is considered important for applications such as ultraviolet-light-emitting diodes, electroluminescent devices, flat-panel displays, sensors and injection lasers [1–5]. At ambient conditions, ZnS shows two polymorphs, zinc blende (cubic) and wurtzite (hexagonal), which have wide band gaps of 3.72 eV and 3.77 eV, respectively [6]. The cubic ZnS is stable at room temperature, whereas the hexagonal ZnS is stable at temperatures higher than 1020 °C. Owing to its large band gap, ZnS doped with some metal cations (including transition metal ions and rare-earth elements) usually exhibits a variety of luminescent properties, such as photoluminescence, electroluminescence, thermoluminescence and triboluminescence [7–10]. Among these materials, ZnS doped with $Mn^{2+}$ ions has been extensively investigated in the past few years [11–14]. Since Mn doping cannot only enhance its optical transition efficiency and increase the number of luminescent centers, but also determine the material to exhibit interesting magneto-optical properties [15–17].

Recently, the size and shape-controlled synthesis of various NCs have attracted widespread attention because of their size and shape-dependent properties and potential applications in various fields. Zhonglin Wang [18] and colleagues reported that the metastable wurtzite-ZnS nanobelts with thickness of ~10 nm surprisingly took an ultrastable wurtzite structure even at high pressure possibly by the size and shape tuning. Alivisatos et al. [19] also pointed out that the shape of semiconductor NCs determined the distribution of the carrier state density and the transport properties of the carrier in crystals. All these investigations suggest that the NCs with controlled properties can be obtained by controlling their size and shape. In this paper, we synthesize ZnS:$Mn^{2+}$ nanoparticles as well as nanorods with cubic and hexagonal structure, respectively, by the solvothermal method. This method requires a relatively low temperature, cheap precursors of low toxicity and makes easy the introduction of transition metal ions such as $Mn^{2+}$, $Cu^{2+}$ etc. into the ZnS lattice. Up to now, the issue about how the structure and morphology affecting the luminescent properties of ZnS:$Mn^{2+}$ NCs has been still blurry. Herein, we will investigate and compare the structure and luminescent properties of ZnS:$Mn^{2+}$ nanoparticles and nanorods, including the local environments surrounding the Mn ions, the optical band gap, photoluminescence excition-emission, the spectra changes induced by the UV light irradiation and the fluorescence decay dynamics.

* Corresponding author. Tel.: +86 434 3290009; fax: +86 434 3294566.
*E-mail address:* jhyang1@jlnu.edu.cn (J. Yang).

0925-3467/$ - see front matter Crown Copyright © 2010 Published by Elsevier B.V. All rights reserved.
doi:10.1016/j.optmat.2010.01.017

## 2. Experimental

ZnS:$Mn^{2+}$ (3%) NCs were prepared by the solvothermal technique. All chemicals (analytical reagents) were purchased from Shanghai Chemical Reagents Co. and used without further purification. Firstly, zinc nitrate [$Zn(NO_3)_2{\cdot}6H_2O$] (0.97 mmol) and manganese nitrate [$Mn(NO_3)_2$] (0.03 mmol) were dissolved in 16 ml ethylenediamine (EN) and water (1:1 in volume ratio); zinc acetate [$Zn(CH_3COO)_2{\cdot}6H_2O$] (0.97 mmol) and manganese acetate [$Mn(CH_3COO)_2{\cdot}4H_2O$] (0.03 mmol) were dissolved in 16 ml ethanol. After stirring for 1 h, thiourea (3 mmol) was put into the resulting complex. After stirring for 2 h, the colloid solution was transferred into two 20-ml Teflon-lined autoclaves and kept at 180 °C for 12 h. After the reaction, the autoclaves were taken out and cooled to room temperature. The products were washed with ethanol and deionized water for several times and separated by centrifugation, and then dried at 80 °C for 1 h to get a white powder.

X-ray diffraction (XRD) patterns were collected on MAC Science MXP-18 X-ray diffractometer using a Cu target radiation source. Transmission electron micrographs (TEMs) were taken with a JEM-2100 electron microscope. The specimen was prepared by depositing a drop of the dilute solution of the sample in 2-propanol on a carbon-coated copper grid and drying at room temperature. The Mn *K*-edge XAFS measurements were performed at room temperature on beamline 1W1B at Beijing Synchrotron Radiation Facility, China. A double crystal Si (1 1 1) monochromator was used, and the signal was collected in fluorescence yield mode with a Lytle ion chamber detector. The data were collected in a mode of sample drain current under a vacuum better than $5 \times 10^{-7}$ Torr. Thermogravimetric analysis (TGA) was performed on Perkin–Elmer Pyris Diamond thermal analyzer under nitrogen atmosphere at a heating rate of 10 °C/min. UV–vis absorption spectra were measured on UV-3101PC UV spectrometer. The specimen was dispersed in ethanol and placed in a 1 cm quartz cell, and ethanol served as the reference. Photoluminescence excitation and emission spectra were recorded at room temperature using Hitachi F-4500 spectrophotometer equipped with a continuous 150-W Xe-arc lamp. Luminescence lifetime was measured with 355 nm light from an $Nd^{3+}$:YAG (yttrium aluminum garnet) laser combined with a third-harmonic generator used as the pump. An oscilloscope was used to record the decay dynamics.

## 3. Results and discussion

The X-ray diffraction patterns of ZnS:$Mn^{2+}$ nanoparticles (NPs) and nanorods (NRs) are shown in Fig. 1a. Three main peaks at 28.45° (1 1 1), 47.41° (220) and 56.29° (311) for NPs can be indexed as cubic zinc blende structure, which are in good agreement with the standard card (JCPDS No. 05-0566). Note that the weak peak centered at 26.95° corresponds to the (1 0 0) diffraction of wurtzite. It shows that the NPs are mainly in zinc blende structure containing a small amount of NPs in wurtzite structure. For NRs, all the diffraction peaks can be well indexed as hexagonal wurtzite structure, which are consistent with the standard card (JCPDS No. 36-1450). Consequently the growth direction could be predicted by comparing the full width at half maximum (FWHM) of different XRD peaks [20]. For NPs, the FWHM has no apparent change among all the diffraction peaks, indicating no change in the structural orientation; For NRs, the (0 0 2) diffraction peak is stronger and narrower than the other peaks, suggesting a preferential growth direction along the *c*-axis. Moreover, the lattice constant '*a*' for cubic and '*a*' and '*c*' for hexagonal structure can be determined from the relations:

$$\text{Cubic}: 1/d_{hkl}^2 = (h^2 + k^2 + l^2)/a^2$$

$$\text{Hexagonal}: 1/d_{hkl}^2 = 4/3\{(h^2 + hk + k^2)/a^2\} + (l^2/c^2)$$

The average lattice constant '*a*' for NPs was found to be 5.415 Å, which is slightly larger than the standard value 5.406 Å, indicating that the as-prepared NPs are under tensile strain. The average lattice constants '*a*' and '*c*' for NRs were found to be $a = 3.831$ and $c = 6.268$ and the corresponding $c/a = 1.636$, which is slightly less than the standard value 1.638, indicating that the NRs are under compressive strain.

The normalized Mn *K*-edge near-edge XAFS (XANES) patterns for NPs and NRs are shown in Fig. 1b, which are in good agreement with the Refs. [21,22]. These near edge features can be reproduced by the FEFF8.2 simulation [23] and the first-principles spin-polarized density functional theory calculation [24] when Mn ions occupy Zn sites in ZnS. These results confirm that Mn ions are incorporated into the ZnS lattice and substitute for the Zn sites, and no Mn-related secondary phase is formed. Note that the local structure of the polymorph of ZnS is the same [22], with tetrahedral coordination for both zinc and sulphur, but different stacking order of {ZnS} layers: ABCA for sphalerite and ABA for wurtzite. Fig. 1c shows the *R*-space extended XAFS (EXAFS) patterns of Mn in NPs and NRs, which can be well compared with the Refs. [25–27]. To interpret the results quantitatively, the curve fitting has been performed. Table 1 lists the corresponding structural parameters. The amplitude of the first peak corresponds to the number of nearest S neighbors around Mn ions. Assuming the standard of four S ions around a Mn ion, the number of S ions in the NPs and NRs were determined to be 3.79 and 3.82, respectively (see Table 1). It is not determined whether the reduction of coordination number is due to the vacancies in the lattice or to the proximity of the Mn ions to the NCs surface. In addition, the width of the first peak corresponds to the Mn–S bond length, as compared with the bulk value of 2.42 Å, the NPs are more disordered than NRs in the first neighbor shell (see Table 1).

Fig. 2 shows the TEM images of NPs and NRs. These NPs with diameters of 10–15 nm (Fig. 2a) are agglomerated, while the NRs are smooth and uniform over their entire lengths and their typical widths are in the range of 8–10 nm (Fig. 2b). In sphalerite ZnS [space group F-43h*m* (No. 216)], the $S^{2-}$ anions form a face-centered cubic arrangement with the $Zn^{2+}$ cations occupying half the tetrahedral holes (vice versa), while in wurtzite ZnS [space group *P*63*mc* (No. 186)], the $S^{2-}$ anions form a hexagonal close-packed lattice along the crystallographic *c*-direction with the $Zn^{2+}$ cations occupying half of the tetrahedral holes. The formation of the cubic NPs is due to their inherent high symmetry in crystallographic structure. The hexagonal NRs, exhibiting preferential growth direction along the *c*-axis, are consistent with their anisotropic wurtzite structure because of the unique structural feature of the (001 h) facet and the existence of a 63-screw axis along the *c*-direction (Donnay–Harker law) [28,29].

The TGA curves of NPs and NRs are shown in Fig. 3. Both NPs and NRs have an initial weight loss at 133 °C corresponding to the weight loss of the adsorbent hydroxyl. At above 623 °C for

**Table 1**
The local structure around Mn ions in NPs and NRs by fitting EXAFS results. $N_{X-S}$: the number of the nearest S around X (X = Zn, Mn) ions; $R_{X-S}$: the radial distance of X–S (X = Zn, Mn).

| Local center | Zn | | Mn | |
|---|---|---|---|---|
| Sample | $N_{Zn-S}$ | $R_{Zn-S}$ (Å) | $N_{Mn-S}$ | $R_{Mn-S}$ (Å) |
| Bulk | 4 | 2.42 ± 0.01 | | |
| NPs | | | 3.79 ± 0.05 | 2.38 ± 0.01 |
| NPs | | | 3.82 ± 0.05 | 2.40 ± 0.01 |

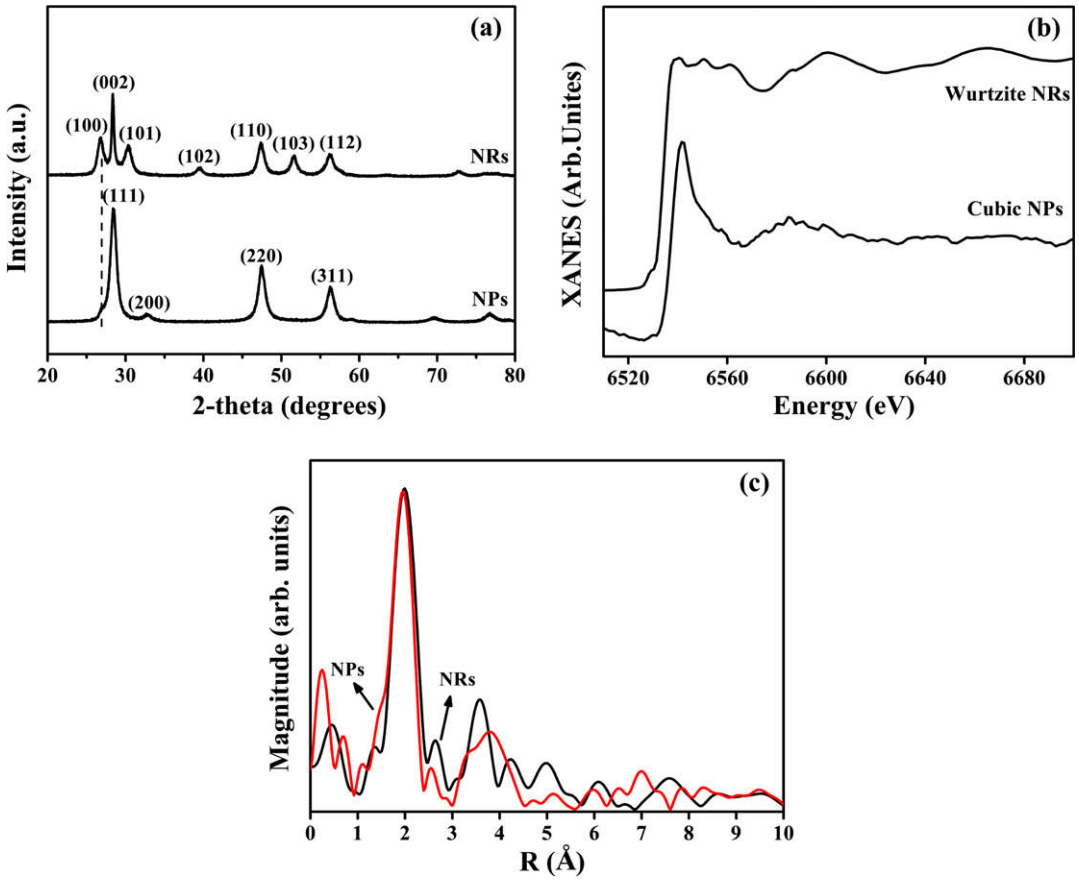


**Fig. 1.** (a) XRD patterns of NPs and NRs (b) Mn *K*-edge XANES patterns of NPs and NRs (c) *R*-space EXAFS patterns of Mn in NPs (red line) and NRs (black line). (For interpretation of the references to colour in this figure legend, the reader is referred to the web version of this article.)

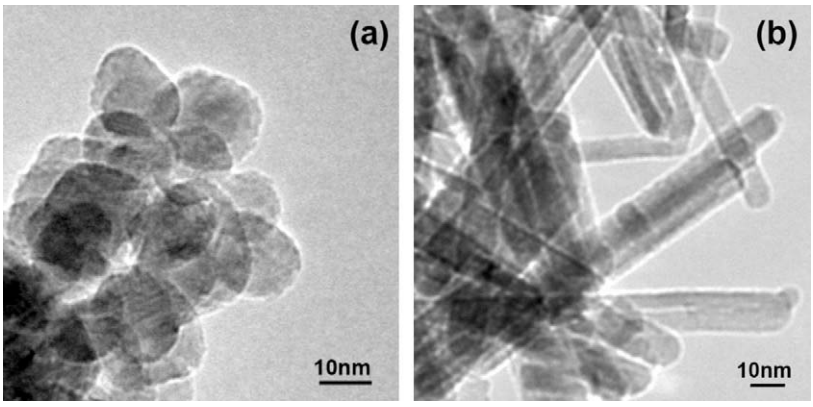


**Fig. 2.** TEM images of (a) NPs (b) NRs.

NRs and 654 °C for NPs, the weight loss may correspond to the decomposition of the ZnS:$Mn^{2+}$ NCs [30]. At 800 °C, there are more residues in the NRs than in NPs. This may be due to the fact that there exist more organic carbon residues trapped on the rod surface. Consequently, during the reaction, the EN-mediated templates are formed on the rod surface by immobilizing of the $NH_2$ containing biomolecules through covalent bonding [31,32].

The optical band gap '*Eg*' can be calculated using the following relation:

$$\alpha = A(h\nu - Eg)^n/h\nu$$

where *A* is a constant and *n* is a constant, equal to 1/2 for the direct band gap semiconductor. The estimated band gaps from the plots of $(\alpha h\nu)^2$ versus $h\nu$ for the NPs and NRs are shown in Fig. 4. The linear nature of the plots indicates the existence of a direct transition. The band gap '*Eg*' is determined by extrapolating the straight portion to the energy axis at $\alpha = 0$. It is found to be 3.83 eV for the NPs and 3.99 eV for the NRs, a 'blueshift' from the normal bulk value of 3.72 eV for cubic ZnS and 3.77 eV for hexagonal ZnS [6]. This may be due to the nanocrystalline nature of the as-prepared NCs, which has been reported in the literatures [33,34].

The photoluminescence excitation-emission spectra of the NPs and NRs can be seen in Fig. 5. The emission spectra were recorded at the excitation wavelength of 344 nm, with an emission filter at 400 nm. Both NPs and NRs show a broad blue–green emission band between 400 and 500 nm, which can be attributed to the defect

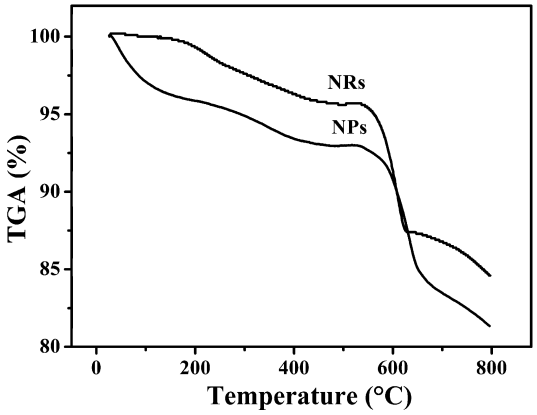


**Fig. 3.** The TGA curves of NPs and NRs.

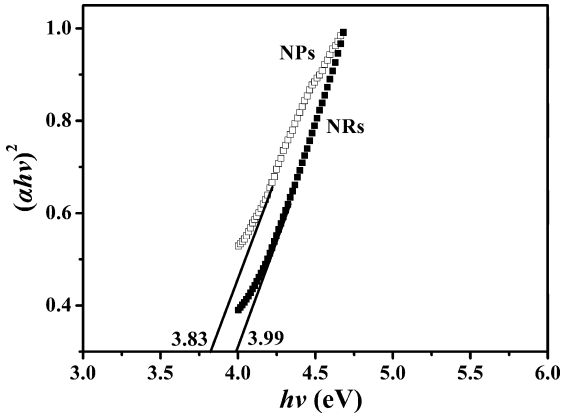


**Fig. 4.** Plots of $(\alpha h\nu)^2$ versus $h\nu$ for NPs (open) and NRs (solid).

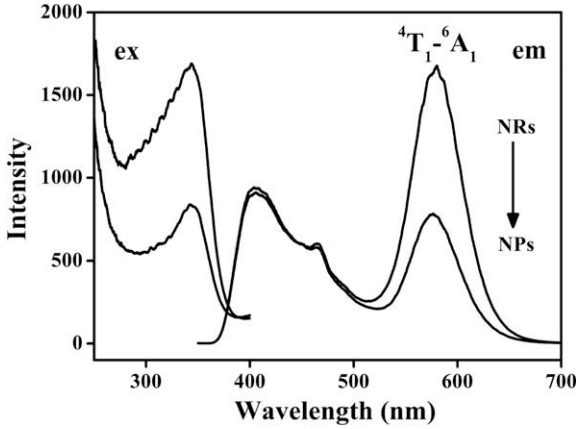


**Fig. 5.** Photoluminescence excitation (left) and emission (right) spectra of NPs and NRs.

states emission [35,36]. The yellow–orange emission centered at 579 nm is caused by the energy transfer of the electron–hole pair excited across the band gap to the Mn d states, in consistent with the previous report [17]. In the PL process, the electron may be captured by the $Mn^{2+}$ ions in the $^4T_1$ level, from which it decays radiatively to the $^6A_1$ level [37]. It is apparent that the location of these emission peaks does not change, but the relative intensity

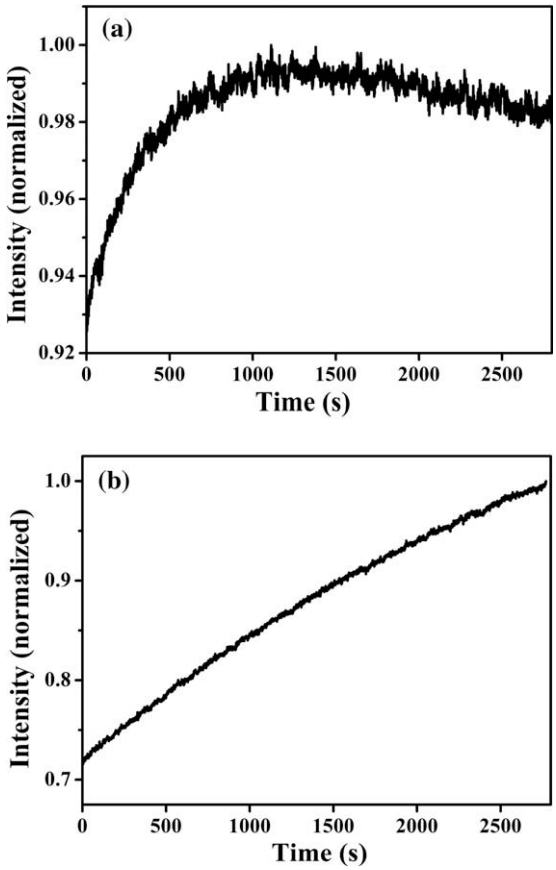


**Fig. 6.** The dependence of the intensity of $Mn^{2+}$ emission on time exposed to the weak UV irradiation (a) NPs and (b) NRs.

of the yellow–orange emission to the defect states related emission is increased from NPs to NRs. Consequently, the intensity of the yellow–orange emission is decided by the energy transfer from the host to $Mn^{2+}$ ions, competing with that to the defect states (primarily surface states) [17]. Wang et al. [18] have reported that the wurtzite-ZnS nanobelts have lower surface energy than the sphalerite ZnS nanoparticles, because the lowest energy plane of the wurtzite structure corresponds to the largest surface of the nanobelts. So, the present results prove that the energy transfer from the host to $Mn^{2+}$ ions for NRs is more efficient than that for NPs due to the lower surface energy of the NRs. In the excitation spectra, the excitonic transition is at 343 nm for NPs and 342 nm for NRs, i.e. at larger wavelengths compared with bulk ZnS (340 nm). Since the diameters of the NPs and NRs are larger than the Bohr exciton diameter of the bulk ZnS (5 nm) [38], the optical behavior of NPs and NRs should be similar to that of the bulk.

The dependence of the intensity of $Mn^{2+}$ emission in NPs and NRs exposed to the weak UV irradiation on time are shown in Fig. 6. The relative change of the intensity in NPs is much larger than that in NRs. This could be explained by the solvents used during the synthesis. Because EN is a very good capping agent that the surface defects on the NRs such as S vacancies are well modified. Under UV exposure, the locally disordered NRs surface becomes relatively ordered, leading to the enhancement of the photoluminescence. Whereas ethanol has no such a strong capping ability as EN, there will be many defect states on the NPs surface [24], which could be responsible for the decrease of the yellow–orange emission.

Fig. 7 shows the fluorescence decay curves of the $^4T_1$–$^6A_1$ transition at 579 nm for NPs and NRs under the 355 nm excitation at

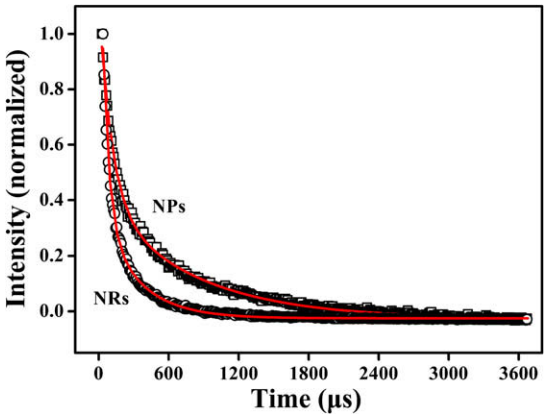


**Fig. 7.** Fluorescence decay curves of the $^4T_1$–$^6A_1$ transition at 579 nm for NPs and NRs under the 355 nm excitation at room temperature.

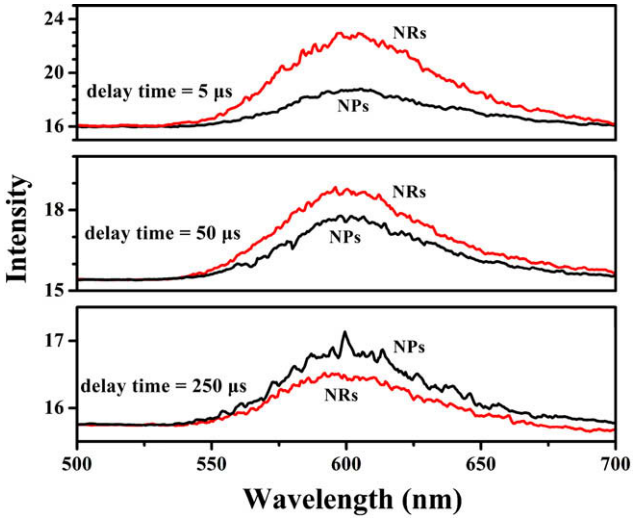


**Fig. 8.** Time-resolved spectra of the $^4T_1$–$^6A_1$ transition at 579 nm of NPs (black line) and NRs (red line) recorded at 355 nm excitation, with delays at 5 μs, 50 μs, 250 μs. (For interpretation of the references to colour in this figure legend, the reader is referred to the web version of this article.)

room temperature. By fitting, the fluorescence lifetime of the $^4T_1$–$^6A_1$ transition was determined to be 0.662 ms for NPs, 0.224 ms for NRs, respectively. Since the lifetime $\tau$ of the excited state is given by the relation $\tau = 1/(K_r + K_n)$, where $K_r$, $K_n$ are the radiative and nonradiative transition rates, respectively, the total electronic transition rate $(K_r + K_n)$ for NRs is faster than that for NPs. To prove this result, we have studied the time behavior of the fluorescence for the NPs and NRs with delays of 5 μs, 50 μs, 250 μs, respectively (Fig. 8). We can clearly observe that the peak evolution of the yellow–orange emission for NRs is faster than that for NPs. The possible explanation may originate in the small change of the crystal field due to the distinct crystal lattice of the NCs. Strains in the lattice or the breakdown of the regular Coulomb potentials on the surface of the NCs may also be the possible reasons [39].

## 4. Conclusions

ZnS:$Mn^{2+}$ nanoparticles and nanorods with cubic and hexagonal structure are successfully synthesized by the solvothermal method. The structure and morphology of the NCs strongly depend on the solvents used during the reaction. The $Mn^{2+}$ ions substitute for the Zn sites in the host ZnS. The surface effect should be responsible for the change of both the relative intensity of the yellow–orange emission to the defect states related emission and the intensity of the $Mn^{2+}$ emission induced by the UV light irradiation. The peak evolution of the yellow–orange emission for NRs is faster than that for NPs, and the fluorescence decay time for the NPs and NRs is 0.662 and 0.224 ms, respectively.

## Acknowledgments

This work was financially supported by the National Natural Science Foundation of China (Grant Nos. 60778040, 60878039, 10904050), National Programs for High Technology Research and Development of China (863) (Item No. 2009AA03Z303), the Science and Technology Bureau of Key Program for Ministry of Education (Item No. 207025) and Cooperation Program between NSRL and BSRF.

## References

[1] Q. Sun, Y. Andrew Wang, L. Li, D. Wang, T. Zhu, J. Xu, C. Yang, Y. Li, Nat. Photon. 1 (2007) 717.
[2] Z. Quan, D. Yang, C. Li, D. Kong, P. Yang, Z. Cheng, J. Lin, Langmuir 25 (2009) 10259.
[3] Y.F. Zhu, D.H. Fan, W.Z. Shen, J. Phys. Chem. C 112 (2008) 10402.
[4] X. Fang, Y. Bando, M. Liao, U.K. Gautam, C. Zhi, B. Dierre, B. Liu, T. Zhai, T. Sekiguchi, Y. Koide, D. Golberg, Adv. Mater. 21 (2009) 2034.
[5] C. Unni, D. Philip, K.G. Gopchandran, Opt. Mater. 32 (2009) 169.
[6] S. Kar, S. Chaudhuri, Chem. Phys. Lett. 414 (2005) 40.
[7] B. Dong, L. Cao, G. Su, W. Liu, H. Qu, D. Jiang, J. Colloid Interf. Sci. 339 (2009) 78.
[8] T. Kang, J. Sung, W. Shim, H. Moon, J. Cho, Y. Jo, W. Lee, B. Kim, J. Phys. Chem. C 113 (2009) 5352.
[9] P. José, J. Beatriz, C. Eloisa, E. Purificación, P. Fabienne, V. Bruno, S. Clément, J. Mater. Chem. 18 (2008) 5193.
[10] M. Zalewska, S. Mahlik, B. Kuklin'ski, M. Grinberg, A.M. Kłonkowski, Opt. Mater. 30 (2008) 719.
[11] V. Wood, J.E. Halpert, M.J. Panzer, M.G. Bawendi, V. Bulovic, Nano Lett. 9 (2009) 2367.
[12] M. Godlewski, A. Wójcik-Głodowska, E. Guziewicz, S. Yatsunenko, A. Zakrzewski, Y. Dumont, E. Chikoidze, M.R. Phillips, Opt. Mater. 31 (2009) 1768.
[13] Y. Fang, S. Chu, H. Chen, P. Kao, I. Chen, C. Hwang, J. Electrochem. Soc. 156 (2009) K55.
[14] T.P. Surkova, V.R. Galakhov, E.Z. Kurmaev, Low Temp. Phys. 35 (2009) 79.
[15] S. Sapra, A. Prakash, A. Ghangrekar, N. Periasamy, D.D. Sarma, J. Phys. Chem. B 109 (2005) 1663.
[16] I. Sarkar, M.K. Sanyal, S. Kar, Phys. Rev. B 75 (2007) 224409.
[17] T. Chanier, F. Virot, R. Hayn, Phys. Rev. B 79 (2009) 205204.
[18] Z. Wang, L. Daemen, Y. Zhao, C.S. Zha, Nat. Mater. 4 (2005) 922.
[19] A.P. Alivisatos, Science 271 (1996) 933.
[20] S. Kar, S. Santra, H. Heinrich, J. Phys. Chem. C 112 (2008) 4036.
[21] J. Pellicer-Porres, A. Segura, J.A. Sans, A.M. Flank, P. Lagarde, A. Polian, Superlattice. Microstruct. 42 (2007) 251.
[22] B. Gilbert, B.H. Frazer, H. Zhang, F. Huang, J.F. Banfield, D. Haskel, J.C. Lang, G. Srajer, G. De Stasio, Phys. Rev. B 66 (2002) 245205.
[23] A.L. Ankudinov, B. Ravel, J.J. Rehr, S.D. Conradson, Phys. Rev. B 58 (1998) 7565.
[24] M. Kunisu, F. Oba, H. Ikeno, I. Tanaka, T. Yamamoto, Appl. Phys. Lett. 86 (2005) 121902.
[25] J. Qi, X. Guo, K. Sakurai, Y. Masumoto, Scripta Mater. 44 (2001) 2315.
[26] A.D. Dinsmore, D.S. Hsu, S.B. Qadri, J.O. Cross, T.A. Kennedy, H.F. Gray, B.R. Ratna, J. Appl. Phys. 88 (2000) 4985.
[27] Y.L. Soo, Z.H. Ming, S.W. Huang, Y.H. Kao, R.N. Baghawa, D. Gallagher, Phys. Rev. B 50 (1994) 7602.
[28] S. Biswas, S. Kar, S. Santra, Y. Jompol, M. Arif, Saiful I. Khondaker, J. Phys. Chem. C 113 (2009) 3617.
[29] X.G. Peng, L. Manna, W.D. Yang, J. Wickham, E. Scher, A. Kadavanich, A.P. Alivisatos, Nature 404 (2000) 59.
[30] H. Song, Y. Leem, B. Kim, Y. Yu, J. Phys. Chem. Solids 69 (2008) 153.
[31] M.V. Limaye, S. Gokhale, S.A. Acharya, S.K. Kulkarni, Nanotechnology 19 (2008) 415602.
[32] X. Chen, H. Xu, N. Xu, F. Zhao, W. Lin, Inorg. Chem. 42 (2003) 3100.
[33] G. Hodes, A.A. Yaran, F. Decker, P. Matsuke, Phys. Rev. B 36 (1987) 4215.
[34] S.S. Kale, C.D. Lokhande, Mater. Chem. Phys. 62 (2000) 103.
[35] S. Biswas, S. Kar, Nanotechnology 19 (2008) 045710.
[36] A. Datta, S.K. Panda, S. Chaudhuri, J. Solid State Chem. 181 (2008) 2332.
[37] R. Maity, K.K. Chattopadhyay, Nanotechnology 15 (2004) 812.
[38] X. Fang, Y. Bando, C. Ye, G. Shen, D. Golberg, J. Phys. Chem. C 111 (2007) 8469.
[39] R. Schmechel, M. Kennedy, H. von Seggern, H. Winkler, M. Kolbe, R.A. Fischer, J. Appl. Phys. 89 (2001) 1679.